48th AIAA Aerospace Sciences Meeting Including the New Horizons Forum and Aerospace Exposition
4 - 7 January 2010, Orlando, Florida

AIAA 2010-109

Delayed-Detached-Eddy Simulation of Shock Wave/Turbulent Boundary Layer Interaction

Patricia X Coronado [*], Baoyuan Wang[†], Ge-Cheng Zha[‡]
Dept. of Mechanical and Aerospace Engineering
University of Miami
Coral Gables, Florida 33124
E-mail: gzha@miami.edu

Abstract

A delayed-detached-eddy simulation (DDES) is conducted with a low diffusion E-CUSP (LDE) scheme and fifth-order WENO scheme for the inviscid fluxes and 4th order central differencing scheme for viscous terms to study the shock/wave turbulent boundary layer interaction. The results show that DDES simulation provides improved results for the shock wave/turbulent boundary layer interaction compared to those of its predecessor the detached-eddy simulation (DES).The computation of mesh refinement indicates that the grid density has significant effects on the results of DES, while being resolved by applying DDES simulation. The computed results of a transonic channel agree well with the experimental data.

1 Introduction

Turbulence modeling is critical when resolving the aerodynamic non-linearity of shock wave/tubulent boundary layer interaction and flow separation. For the simulation of turbulent flows, methods based on Reynolds average Navier-Strokes (RANS) equations are widely used, although they are not able to simulate flow separation in an accurate manner. This is because RANS methods calculate the large scale eddies using a universal model. Such universal model does not exist for the large scale turbulence that is affected by flow geometry and boundary conditions.

Performing better than the RANS model, Large Eddy Simulation (LES) is promising while overcoming the RANS model disadvantages. In LES, the governing equations are spatially filtered on the scale of the numerical grid. The large energy containing scales are directly simulated, and the small scale eddies, which are generally more homogeneous and universal, are modeled. The large eddies are strongly affected by the flow field geometry boundaries, therefore the direct computation of the large eddies by LES is more accurate than modeling the large eddies by RANS. The effect of the unresolved small scales of motion in LES is modeled by a subgrid-scale (SGS) model[1][2][3][4][5] or by the inherent dissipation in the numerical schemes[6][7][8][9][10][11][12]. Because the statistics of the small scale turbulence are more isotropic and universal, a general physical model for small scale eddies is more plausible.

---

[*] Graduate Student, AIAA Member

[†] Ph.D., AIAA Member

[‡] Associate Professor, AIAA Senior Member

1.1 Detached-Eddy-Simulation

For high Reynolds number flows such as those of turbo-machinery blades and transonic wings, to resolve the wall boundary layer, LES needs the CPU resource not much less than the Direct Numerical Simulation(DNS). This makes the LES too expensive for high Reynolds number flow calculations and therefore it is not hopeful for LES to be rigorously implemented for another 4 decades in engineering applications [13]. Spalart et al. developed the so called detached-eddy simulation (DES) strategy[13], which is a hybrid RANS and LES method, to overcome the intensive CPU requirement for LES. Near the solid surface within the wall boundary layer, the unsteady RANS model is realized. Away from the wall surface, the model automatically converts to LES. By using the RANS model near the wall, the fine mesh resolution of LES to resolve the viscous sublayer is avoided and the CPU time can be tremendously reduced. The motivation of DES is that the LES is powerful in regions of massive separation and other free shear flows such as jets, but is much too costly in the large area of thin wall boundary layers.

In 2001, Spalart gave a grid guidance for DES [14, 15], which divides a flow domain with solid walls to Euler region, LES region, and RANS region. The LES region is composed of Viscous, Focus and Departure region. In the RANS region, the domain is further divided to Viscous region and Outer region. Spalart's DES grid guidance gives sufficient grid resolution for LES region and the transition to Euler region from RANS region. The grid size is dramatically reduced compared to the pure LES.

Even though the DES concept is much newer than RANS and LES concept, its application for turbulence simulation has already achieved encouraging success as shown in the work of Wang[16][17] and Tarvin et al. (1999) [18], Spalart (2001)[14, 15], Forsythe et al.(2002)[19], Viswanathan et al. [20], Squires et al.[21, 22], Hsnsen, et al. (2003)[23], Subbareddy et al. (2005) [24]. These flows calculated using DES include those for airfoils, cylinders, forbodies, base flows, etc. The results are qualitatively and quantitatively better than the solutions using RANS. DES appears to be a suitable compromise between the physical models of turbulence and CPU efficiency. In those DES applications, almost all the algorithms use 2nd order accuracy except that of Tarvin et al. (1999) [18], which employs fifth order upwind scheme for the inviscid convective terms in space.

1.2 Delayed-Detached-Eddy Simulation

However, with the spread of the successful DES application after it was first proposed in 1997, a defect of the first generation DES model(DES97) [13] has been also exposed, being that the transition from the RANS model to LES in DES97 may not be grid spacing independent[25]. DES is originally designed to treat the entire boundary layer using a RANS model and to use LES for separated flow regions. A fine mesh with grid spacing much smaller than the boundary layer thickness may exhibit an incorrect behavior in boundary layers and shallow separation regions due to locating the RANS/LES transition within the boundary layer. The grid spacing could be fine enough for the DES length scale to follow the LES branch, which will lower the eddy viscosity below the RANS level. The resolved Reynolds stresses determined from the velocity fluctuation (LES content) may be lacking because the resolution is not fine enough to fully support it. The DES limiter then reduces the eddy viscosity, and therefore the modeled Reynolds stresses. This phenomenon is referred as modeled-stress depletion (MSD)[25]. This drawback is also considered as one of the possible causes for the inaccurate prediction of flow separation region size with suction flow control when the DES is used as indicated by Rumsey [26].

To overcome the MSD problem and make the DES limiter independent of grid spacing, Spalart suggested a modification to the original DES97 model in 2006[25], referred to as Delayed-Detached-Eddy Simulation (DDES). A blending function similar to the one used by Menter and Kuntz [27] for the SST model is introduced to limit the DES length scale to ensure the transition of RANS to LES be independent of grid spacing. The DDES model has demonstrated excellent agreement with experiment and a significant improvement over the DES97 for the tested cases, which include a flat plat boundary layer resolved with mesh spacing significantly smaller than the boundary layer thickness, a circular cylinder, a single airfoil with weak separation near trailing edge, the backward facing step with large separation region, and a multi-element airfoil. The predicted separation onset and separation region length agree well with the experiments.

In this paper, the DDES of Spalart[25] based on the Spalart-Allmaras one equation turbulence model will be employed with the recently developed low diffusion E-CUSP scheme[28] with fifth-order WENO scheme for the inviscid fluxes and 4th order central differencing scheme for viscous terms[29, 30, 31, 32, 33, 11], in order to investigate the shock wave/turbulet boundary layer interaction.

2 Governing Equations

The governing equations for the flow field computation are the spatially filtered 3D general Navier-Stokes equations in generalized coordinates and can be expressed as follows:

$$\frac{\partial \mathbf{Q}'}{\partial t} + \frac{\partial \mathbf{E}'}{\partial \xi} + \frac{\partial \mathbf{F}'}{\partial \eta} + \frac{\partial \mathbf{G}'}{\partial \zeta} = \frac{1}{\mathrm{Re}} \left(\frac{\partial \mathbf{E}'_{\mathbf{v}}}{\partial \xi} + \frac{\partial \mathbf{F}'_{\mathbf{v}}}{\partial \eta} + \frac{\partial \mathbf{G}'_{\mathbf{v}}}{\partial \zeta} \right) \tag{1}$$

where Re is the Reynolds number, and

$$\mathbf{Q}' = \frac{\mathbf{Q}}{J} \tag{2}$$

$$\mathbf{E}' = \frac{1}{J}(\xi_t \mathbf{Q} + \xi_x \mathbf{E} + \xi_y \mathbf{F} + \xi_z \mathbf{G}) \tag{3}$$

$$\mathbf{F}' = \frac{1}{J}(\eta_t \mathbf{Q} + \eta_x \mathbf{E} + \eta_y \mathbf{F} + \eta_z \mathbf{G}) \tag{4}$$

$$\mathbf{G}' = \frac{1}{J}(\zeta_t \mathbf{Q} + \zeta_x \mathbf{E} + \zeta_y \mathbf{F} + \zeta_z \mathbf{G}) \tag{5}$$

$$\mathbf{E}'_{\mathbf{v}} = \frac{1}{J}(\xi_x \mathbf{E}_{\mathbf{v}} + \xi_y \mathbf{F}_{\mathbf{v}} + \xi_z \mathbf{G}_{\mathbf{v}}) \tag{6}$$

$$\mathbf{F}'_{\mathbf{v}} = \frac{1}{J}(\eta_x \mathbf{E}_{\mathbf{v}} + \eta_y \mathbf{F}_{\mathbf{v}} + \eta_z \mathbf{G}_{\mathbf{v}}) \tag{7}$$

$$\mathbf{G}'_{\mathbf{v}} = \frac{1}{J}(\zeta_x \mathbf{E}_{\mathbf{v}} + \zeta_y \mathbf{F}_{\mathbf{v}} + \zeta_z \mathbf{G}_{\mathbf{v}}) \tag{8}$$

where J is the transformation Jacobian. The variable vector $\mathbf{Q}$, and inviscid flux vectors $\mathbf{E}$, $\mathbf{F}$, and $\mathbf{G}$ are given as the following.

$$\mathbf{Q}=\begin{pmatrix}\bar\rho\\ \bar\rho\tilde u\\ \bar\rho\tilde v\\ \bar\rho\tilde w\\ \bar\rho\tilde e\end{pmatrix},\ \mathbf{E}=\begin{pmatrix}\bar\rho\tilde u\\ \bar\rho\tilde u^2+\bar p\\ \bar\rho\tilde u\tilde v\\ \bar\rho\tilde u\tilde w\\ (\bar\rho\tilde e+\bar p)\tilde u\end{pmatrix},\ \mathbf{F}=\begin{pmatrix}\bar\rho\tilde v\\ \bar\rho\tilde v\tilde u\\ \bar\rho\tilde v^2+\bar p\\ \bar\rho\tilde v\tilde w\\ (\bar\rho\tilde e+\bar p)\tilde v\end{pmatrix},\ \mathbf{G}=\begin{pmatrix}\bar\rho\tilde w\\ \bar\rho\tilde w\tilde u\\ \bar\rho\tilde w\tilde v\\ \bar\rho\tilde w^2+\bar p\\ (\bar\rho\tilde e+\bar p)\tilde w\end{pmatrix}$$

The inviscid fluxes in generalized coordinate system are expressed as:

$$\mathbf{E}'=\begin{bmatrix}\bar\rho U\\ \bar\rho\tilde u U+l_x\bar p\\ \bar\rho\tilde v U+l_y\bar p\\ \bar\rho\tilde w U+l_z\bar p\\ (\bar\rho\tilde e+\bar p)\,U-l_t\bar p\end{bmatrix},\ \mathbf{F}'=\begin{bmatrix}\bar\rho V\\ \bar\rho\tilde u V+m_x\bar p\\ \bar\rho\tilde v V+m_y\bar p\\ \bar\rho\tilde w V+m_z\bar p\\ (\bar\rho\tilde e+\bar p)\,V-m_t\bar p\end{bmatrix},\ \mathbf{G}'=\begin{bmatrix}\bar\rho W\\ \bar\rho\tilde u W+n_x\bar p\\ \bar\rho\tilde v W+n_y\bar p\\ \bar\rho\tilde w W+n_z\bar p\\ (\bar\rho\tilde e+\bar p)\,W-n_t\bar p\end{bmatrix}$$

where U, V and W are the contravariant velocities in ξ, η and ζ directions.

$$\begin{aligned}U&=l_t+\mathbf{l}\bullet\mathbf{V}=l_t+l_x\tilde u+l_y\tilde v+l_z\tilde w\\ V&=m_t+\mathbf{m}\bullet\mathbf{V}=m_t+m_x\tilde u+m_y\tilde v+m_z\tilde w\\ W&=n_t+\mathbf{n}\bullet\mathbf{V}=n_t+n_x\tilde u+n_y\tilde v+n_z\tilde w\end{aligned}\tag{9}$$

$\mathbf{l}$, $\mathbf{m}$, $\mathbf{n}$ are the normal vectors on ξ,η,ζ surfaces with their magnitudes equal to the elemental surface area and pointing to the directions of increasing ξ,η,ζ.

$$\mathbf{l}=\frac{\nabla\xi}{J},\ \mathbf{m}=\frac{\nabla\eta}{J},\ \mathbf{n}=\frac{\nabla\zeta}{J}\tag{10}$$

$$l_t=\frac{\xi_t}{J},\ m_t=\frac{\eta_t}{J},\ n_t=\frac{\zeta_t}{J}\tag{11}$$

$$\mathbf{E_v}=\begin{pmatrix}0\\ \bar\tau_{xx}+\sigma_{xx}\\ \bar\tau_{xy}+\sigma_{xy}\\ \bar\tau_{xz}+\sigma_{xz}\\ Q_x\end{pmatrix},\ \mathbf{F_v}=\begin{pmatrix}0\\ \bar\tau_{yx}+\sigma_{yx}\\ \bar\tau_{yy}+\sigma_{yy}\\ \bar\tau_{yz}+\sigma_{yz}\\ Q_y\end{pmatrix},\ \mathbf{G_v}=\begin{pmatrix}0\\ \bar\tau_{zx}+\sigma_{zx}\\ \bar\tau_{zy}+\sigma_{zy}\\ \bar\tau_{zz}+\sigma_{zz}\\ Q_z\end{pmatrix},$$

In the above equations, ρ is the density, u,v,w are the Cartesian velocity components in x,y,z directions, p is the static pressure, and e is the total energy per unit mass. The overbar denotes a regular filtered variable, and the tilde is used to denote the Favre filtered variable. The $\bar\tau$ is the molecular viscous stress tensor and is estimated as:

$$\bar\tau_{ij}=\frac{2}{3}\tilde\mu\frac{\partial\tilde u_k}{\partial x_{\ k}}\delta_{ij}+\mu(\frac{\partial\tilde u_i}{\partial x_j}+\frac{\partial\tilde u_j}{\partial x_i}),\qquad i,j=1,2,3\tag{12}$$

The above equation is in the tensor form, where the subscript 1, 2, 3 represent the coordinates, x,y,z and the Einstein summation convention is used.

The molecular viscosity $\tilde\mu=\tilde\mu(\tilde T)$ is determined by Sutherland law.

The σ is the subgrid scale stress tensor due to the filtering process and is expressed as:

$$\sigma_{ij} = -\bar{\rho}(\widetilde{u_i u_j} - \tilde{u}_i \tilde{u}_j) \tag{13}$$

The energy flux Q is expressed as:

$$Q_i = \tilde{u}_j(\bar{\tau}_{ij} + \sigma_{ij}) - \bar{q}_i + \Phi_i \tag{14}$$

where Φ is the subscale heat flux:

$$\Phi_i = -C_p \bar{\rho}(\widetilde{u_i T} - \tilde{u}_i \tilde{T}) \tag{15}$$

The $\bar{q}_i$ is the molecular heat flux:

$$\bar{q}_i = -\frac{C_p \tilde{\mu}}{Pr} \frac{\partial \tilde{T}}{\partial x_i} \tag{16}$$

$$\bar{\rho}\tilde{e} = \frac{\bar{p}}{(\gamma - 1)} + \frac{1}{2}\bar{\rho}(\tilde{u}^2 + \tilde{v}^2 + \tilde{w}^2) + \rho k \tag{17}$$

where γ is the ratio of specific heats, ρk is the subscale kinetic energy per unit volume.

$$\rho k = \frac{1}{2}\bar{\rho}(\widetilde{u_i u_i} - \tilde{u}_i \tilde{u}_i) = -\frac{1}{2}\sigma_{ii} \tag{18}$$

In the present calculation, the ρk in Eq.(17) is omitted based on the assumption that the effect is small.

3 Detached-Eddy Simulation

The Navier-Stokes equations can then be solved using the DES model suggested by Spalart et al. [13] as the following.

First the sub-grid scale stresses are determined as:

$$\sigma_{ij} = \mu_{DES}\left(\frac{\partial \tilde{u}_i}{\partial x_j} + \frac{\partial \tilde{u}_j}{\partial x_i} - \frac{2}{3}\frac{\partial \tilde{u}_k}{\partial x_k}\delta_{ij}\right) - \frac{2}{3}\rho k \delta_{ij} \qquad i, j = 1, 2, 3 \tag{19}$$

The turbulent heat flux will be evaluated as:

$$\Phi_i = C_p \frac{\mu_{DES}}{Pr_t} \frac{\partial \tilde{T}}{\partial x_i} \tag{20}$$

where

$$\mu_{DES} = \rho \nu_t = \rho \tilde{\nu} f_{v1} \tag{21}$$

$\tilde{\nu}$ is a working variable and is determined by the following Spalart-Allmaras model[34][13][20][35]:

$$\frac{D\tilde{\nu}}{Dt} = c_{b1}\tilde{S}\tilde{\nu}\left(1-f_{t2}\right) - [c_{w1}f_w - \frac{c_{b1}}{k^2}f_{t2}][\frac{\tilde{\nu}}{d}]^2 + \frac{1}{\sigma}[\nabla\cdot((\nu+\tilde{\nu})\nabla\tilde{\nu}) + c_{b2}(\nabla\tilde{\nu})^2] + f_{t1}\left(\Delta q\right)^2 \tag{22}$$

In generalized coordinate system, the conservative form of Eq.(22) is given as the following:

$$\begin{aligned} \frac{\partial\frac{1}{J}\rho\tilde{\nu}}{\partial t} + \frac{\partial\rho\tilde{\nu}U}{\partial\xi} + \frac{\partial\rho\tilde{\nu}V}{\partial\eta} + \frac{\partial\rho\tilde{\nu}W}{\partial\zeta} = \frac{1}{Re}\Bigg(&\frac{\partial\frac{\rho}{\sigma}\left(\nu+\tilde{\nu}\right)\left(\mathbf{l}\bullet\nabla\tilde{\nu}\right)}{\partial\xi} \\ .+\frac{\partial\frac{\rho}{\sigma}\left(\nu+\tilde{\nu}\right)\left(\mathbf{m}\bullet\nabla\tilde{\nu}\right)}{\partial\eta} &+ \frac{\partial\frac{\rho}{\sigma}\left(\nu+\tilde{\nu}\right)\left(\mathbf{n}\bullet\nabla\tilde{\nu}\right)}{\partial\zeta} + \frac{1}{J}S_\nu\Bigg) \end{aligned} \tag{23}$$

where

$$\begin{aligned} S_\nu = \rho C_{b1}\left(1-f_{t2}\right)\tilde{S}\tilde{\nu} + \tfrac{1}{Re}\Big[-\rho\left(C_{w1}f_w - \tfrac{C_{b1}}{\kappa^2}f_{t2}\right)\left(\tfrac{\tilde{\nu}}{d}\right)^2 \\ +\tfrac{\rho}{\sigma}C_{b2}\left(\nabla\tilde{\nu}\right)^2 - \tfrac{1}{\sigma}\left(\nu+\tilde{\nu}\right)\nabla\tilde{\nu}\bullet\nabla\rho\Big] + Re\left[\rho f_{t1}\left(\Delta q\right)^2\right] \end{aligned} \tag{24}$$

Eq.(23) is coupled with Eq.(1) when it is solved.

The eddy viscosity ν_t is obtained from:

$$\nu_t = \tilde{\nu}f_{v1} \qquad f_{v1} = \frac{\chi^3}{\chi^3 + c_{v1}^3} \qquad \chi = \frac{\tilde{\nu}}{\nu} \tag{25}$$

where ν is the molecular viscosity. The production term is:

$$\tilde{S} = S + \frac{\tilde{\nu}}{k^2 d^2}f_{v2}, \qquad f_{v2} = 1 - \frac{\chi}{1+\chi f_{v1}} \tag{26}$$

where S is the magnitude of the vorticity. The function f_w is given by

$$f_w = g(\frac{1+c_{w3}^6}{g^6 + c_{w3}^6})^{1/6}, \qquad g = r + c_{w2}(r^6 - r), \qquad r = \frac{\tilde{\nu}}{\tilde{S}k^2 d^2} \tag{27}$$

The function f_{t2} is given by

$$f_{t2} = C_{t3}exp\left(-C_{t4}\chi^2\right) \tag{28}$$

and the trip function f_{t1} is

$$f_{t1} = C_{t1}g_t exp\left[-C_{t2}\frac{\omega_t^2}{\Delta U^2}\left(d^2 + g_t^2 d_t^2\right)\right],\ g_t = min\left(0.1, \frac{\Delta q}{\omega_t \Delta x_t}\right) \tag{29}$$

where, ω_t is the wall vorticity at the wall boundary layer trip location, d is the distance to the closest wall, d_t is the distance of the field point to the trip location, Δq is the difference of the velocities between the field point and the trip location, Δx_t is the grid spacing along the wall at the trip location.

The values of the coefficients are: $c_{b1} = 0.1355, c_{b2} = 0.622, \sigma = \frac{2}{3}, c_{w1} = \frac{c_{b1}}{k^2} + (1 + c_{b2})/\sigma, c_{w2} = 0.3, c_{w3} = 2, k = 0.41, c_{v1} = 7.1, c_{t1} = 1.0, c_{t2} = 2.0, c_{t3} = 1.1, c_{t4} = 2.0.$

In DES, c_{t1} and c_{t3} are set as zero. The distance to the nearest wall, d, is replaced by $\tilde{d}$ as

$$\tilde{d} = min(d, C_{DES}\Delta) \tag{30}$$

where Δ is the largest spacing of the grid cell in all the directions.

Within the boundary layer close to walls, $\tilde{d} = d$, hence the turbulence is simulated by the RANS mode determined by the Spalart-Allmaras model[34]. Away from the boundary layer, $\tilde{d} = C_{DES}\Delta$ is most of the cases. When the production and destruction terms of the model are balanced, the length scale $\tilde{d}$ will have a Smagorinsky-like eddy viscosity and the turbulence is simulated by the LES model. Analogous to the classical LES theory, the length scale Δ is to cascade the energy to the grid size. The coefficient $C_{DES} = 0.65$ is used as set in the homogeneous turbulence[36]. The Pr_t may take the value of 0.9 within the boundary layer for RANS mode and 0.5 for LES mode away from the wall surface. Eq.(22) will be extended to generalized coordinates and will be coupled and solved together with the filtered Navier-Stokes equations, Eq.(1).

4 Delayed-Detached-Eddy Simulation

The DDES formulation introduced by Sparlat et al.[25] suggests some modifications to his previous DES model[13], given that in wide boundary layers and shallow separation regions the DES simulation can present an erroneous behavior. This may occur when the thickness of the boundary layer is greater than the grid spacing parallel to the wall, making the transition from RANS to LES earlier. With the new modified DDES, the RANS model is retained longer for thick boundary layers independent of the grid spacing. The DES model is adjusted as follows.

The parameter r is modified from the S-A definition to:

$$r_d = \frac{\nu_t + \nu}{(U_{i,j}U_{i,j})^{0.5}k^2d^2} \tag{31}$$

where $U_{i,j}$ are the velocity gradients, and the subscript d refers to delayed for DDES. This parameter is modified in this form so it can be applied to any eddy-viscous model.

r_d is applied in the following function

$$f_d = 1 - tanh([8r_d]^3) \tag{32}$$

The coefficients 8 and 3 are acquired from DDES flat plate boundary layer tests[25] by matching the solution to the RANS values. In this way the DES $\tilde{d}$ can be modified and be definied for DDES as follows:

$$\tilde{d} = d - f_d max(0, d - C_{DES}\Delta) \tag{33}$$

This modification in $\tilde{d}$ reduces the grey transition area between RANS and LES. The qualitative change of the new $\tilde{d}$ is very significant, depending now on the eddy-viscosity field. The DDES model now can refuse the transition to LES if not ready, when the function f_d, using the value of r_d, indicates that the point still lies within the boundary layer. The opposite also occurs, when there is massive separation indicated by f_d, the change from RANS to LES takes place in the simulation.

For simplicity, all the overbar and tilde in above equations will be dropped in the rest of this paper.

5 The Numerical Method

5.1 The Low Diffusion E-CUSP (LDE) Scheme[28]

The basic idea of the LDE scheme suggested by Zha et al.[28] is to split the inviscid flux into the convective flux E^c and the pressure flux E^p. With the one extra equation from the S-A model for DES, the splitting is basically the same as the original scheme for the Euler equation and is straightforward[37]. This is an advantage over the Roe scheme[38], for which the eigenvectors need to be derived when any extra equation is added to the governing equations. In [39], the LDE scheme is shown to be more efficient than the Roe scheme when the S-A one equation turbulence model is coupled.

In generalized coordinate system, the flux $\mathbf{E}$ can be split as the following:

$$\mathbf{E}' = E^c + E^p = \begin{pmatrix} \rho U \\ \rho u U \\ \rho v U \\ \rho w U \\ \rho e U \\ \rho \tilde{\nu} U \end{pmatrix} + \begin{pmatrix} 0 \\ l_x p \\ l_y p \\ l_z p \\ p\overline{U} \\ 0 \end{pmatrix} \tag{34}$$

where, U is the contravariant velocity in ξ direction and is defined as the following:

$$U = l_t + l_x u + l_y v + l_z w \tag{35}$$

$\overline{U}$ is defined as:

$$\overline{U} = l_x u + l_y v + l_z w \tag{36}$$

The convective term, E^c is evaluated by

$$E^c = \rho U \begin{pmatrix} 1 \\ u \\ v \\ w \\ e \\ \tilde{\nu} \end{pmatrix} = \rho U f^c, \ f^c = \begin{pmatrix} 1 \\ u \\ v \\ w \\ e \\ \tilde{\nu} \end{pmatrix} \tag{37}$$

let

$$C = c\left(l_x^2 + l_y^2 + l_z^2\right)^{\frac{1}{2}} \tag{38}$$

where $c = \sqrt{\gamma R T}$ is the speed of sound. Then the convective flux at interface $i + \frac{1}{2}$ is evaluated as:

$$E^c_{i+\frac{1}{2}} = C_{\frac{1}{2}}\left[\rho_L C^+ f^c_L + \rho_R C^- f^c_R\right] \tag{39}$$

where, the subscripts L and R represent the left and right hand sides of the interface. The Mach number splitting of Edwards[40, 41] is borrowed to determine c^+ and c^- as the following:

$$\begin{aligned}
&C_{\frac{1}{2}} = \tfrac{1}{2}\left(C_L + C_R\right),\ C^+ = \alpha^+_L\left(1 + \beta_L\right) M_L - \beta_L M^+_L - M^+_{\frac{1}{2}} \\
&C^- = \alpha^-_R\left(1 + \beta_R\right) M_R - \beta_R M^-_R + M^-_{\frac{1}{2}} \\
&M_L = \tfrac{U_L}{C_{\frac{1}{2}}},\ M_R = \tfrac{U_R}{C_{\frac{1}{2}}} \\
&\alpha_{L,R} = \tfrac{1}{2}\left[1 \pm sign\left(M_{L,R}\right)\right] \\
&\beta_{L,R} = -max\left[0, 1 - int\left(|M_{L,R}|\right)\right] \\
&M^+_{\frac{1}{2}} = M_{\frac{1}{2}}\tfrac{C_R + C_L\Phi}{C_R + C_L},\ M^-_{\frac{1}{2}} = M_{\frac{1}{2}}\tfrac{C_L + C_R\Phi^{-1}}{C_R + C_L},\ \Phi = \tfrac{\left(\rho C^2\right)_R}{\left(\rho C^2\right)_L} \\
&M_{\frac{1}{2}} = \beta_L \delta^+ M^-_L - \beta_R \delta^- M^+_R \\
&M^\pm_{L,R} = \pm\tfrac{1}{4}\left(M_{L,R} \pm 1\right)^2 \\
&\delta^\pm = \tfrac{1}{2}\left\{1 \pm sign\left[\tfrac{1}{2}\left(M_L + M_R\right)\right]\right\}
\end{aligned}$$

The pressure flux, E^p is evaluated as the following

$$E^p_{i+\frac{1}{2}} = \begin{pmatrix} 0 \\ \mathcal{P}^+ p\, l_x \\ \mathcal{P}^+ p\, l_y \\ \mathcal{P}^+ p\, l_z \\ \frac{1}{2}p\left[\overline{U} + \overline{C}_{\frac{1}{2}}\right] \\ 0 \end{pmatrix}_L + \begin{pmatrix} 0 \\ \mathcal{P}^- p\, l_x \\ \mathcal{P}^- p\, l_y \\ \mathcal{P}^- p\, l_z \\ \frac{1}{2}p\left[\overline{U} - \overline{C}_{\frac{1}{2}}\right] \\ 0 \end{pmatrix}_R \tag{40}$$

The contravariant speed of sound $\overline{C}$ in the pressure vector is consistent with $\overline{U}$. It is computed based on C as the following,

$$\overline{C} = C - l_t \tag{41}$$

The use of $\overline{U}$ and $\overline{C}$ instead of U and C in the pressure vector is to take into account of the grid speed so that the flux will transit from subsonic to supersonic smoothly. When the grid is stationary, $l_t = 0$, $\overline{C} = C$, $\overline{U} = U$.

The pressure splitting coefficient is:

$$\mathcal{P}^{\pm}_{L,R} = \frac{1}{4}\left(M_{L,R} \pm 1\right)^2 \left(2 \mp M_L\right) \tag{42}$$

The LDE scheme can capture crisp shock profile and exact contact surface discontinuities as accurately as the Roe scheme[28]. However, it is simpler and more CPU efficient than the Roe scheme due to no matrix operation.

5.2 The Fifth-Order WENO Scheme

The interface flux, $E_{i+\frac{1}{2}} = E(Q_L, Q_R)$, is evaluated by determining the conservative variables Q_L and Q_R using fifth-order WENO scheme[30]. For example,

$$\left(Q_L\right)_{i+\frac{1}{2}} = \omega_0 q_0 + \omega_1 q_1 + \omega_2 q_2 \tag{43}$$

where

$$\begin{aligned} q_0 &= \tfrac{1}{3}Q_{i-2} - \tfrac{7}{6}Q_{i-1} + \tfrac{11}{6}Q_i \\ q_1 &= -\tfrac{1}{6}Q_{i-1} + \tfrac{5}{6}Q_i + \tfrac{1}{3}Q_{i+1} \\ q_2 &= \tfrac{1}{3}Q_i + \tfrac{5}{6}Q_{i+1} - \tfrac{1}{6}Q_{i+2} \end{aligned} \tag{44}$$

$$\omega_k = \frac{\alpha_k}{\alpha_0 + \ldots + \alpha_{r-1}} \tag{45}$$

$$\begin{aligned} &\alpha_k = \tfrac{C_k}{\epsilon + IS_k},\ k = 0, \ldots, r-1 \\ &C_0 = 0.1,\ C_1 = 0.6,\ C_2 = 0.3 \\ &IS_0 = \tfrac{13}{12}\left(Q_{i-2} - 2Q_{i-1} + Q_i\right)^2 + \tfrac{1}{4}\left(Q_{i-2} - 4Q_{i-1} + 3Q_i\right)^2 \\ &IS_1 = \tfrac{13}{12}\left(Q_{i-1} - 2Q_i + Q_{i+1}\right)^2 + \tfrac{1}{4}\left(Q_{i-1} - Q_{i+1}\right)^2 \\ &IS_2 = \tfrac{13}{12}\left(Q_i - 2Q_{i+1} + Q_{i+2}\right)^2 + \tfrac{1}{4}\left(3Q_i - 4Q_{i+1} + Q_{i+2}\right)^2 \end{aligned} \tag{46}$$

where, ϵ is originally introduced to avoid the denominator becoming zero and is supposed to be a very small number. In [30], it is observed that IS_k will oscillate if ϵ is too small and also shift the weights away from the optimal values in the smooth region. The higher the ϵ values, the closer the weights approach the optimal values, C_k, which will give the symmetric evaluation of the interface flux with minimum numerical dissipation. When there are shocks in the flow field, ϵ can not be too large to maintain the sensitivity to shocks. In [30], $\epsilon = 10^{-2}$ is recommended for the transonic flow with shock waves.

The viscous terms are discretized by a conservative fourth-order accurate finite central differencing scheme developed by Shen et al[30]. This central differencing scheme is constructed to how the stencil width within the stencil width of the WENO scheme.

$$\frac{\partial R}{\partial \xi}|_i = \tilde{R}_{i+1/2} - \tilde{R}_{i-1/2} \tag{47}$$

where

$$\tilde{R}_{i-1/2} = \frac{1}{24\Delta\xi}(-R_{i+1/2} + 26R_{i-1/2} - R_{i-3/2}) \tag{48}$$

$$R_{i-1/2} = \left[(\xi_x \tau_{xx}) + (\eta_y \tau_{xy}) + (\zeta_z \tau_{xz})\right]_{i-1/2}$$

$$\begin{aligned}(\tau_{xx})_{i-1/2} = \quad & \mu|_{i-1/2}\{\tfrac{4}{3}\left[(\xi_x \tfrac{\partial u}{\partial \xi})|_{i-1/2} + (\eta_x \tfrac{\partial u}{\partial \eta})|_{i-1/2} + (\zeta_x \tfrac{\partial u}{\partial \zeta})|_{i-1/2}\right] \\ & -\tfrac{2}{3}[(\xi_y \tfrac{\partial v}{\partial \xi})|_{i-1/2} + (\eta_y \tfrac{\partial v}{\partial \eta})|_{i-1/2} + (\zeta_y \tfrac{\partial v}{\partial \zeta})|_{i-1/2} \\ & (\xi_z \tfrac{\partial w}{\partial \xi})|_{i-1/2} + (\eta_z \tfrac{\partial w}{\partial \eta})|_{i-1/2} + (\zeta_z \tfrac{\partial w}{\partial \zeta})|_{i-1/2}]\}\end{aligned} \tag{49}$$

If R in Eq.(48) can be approximated with the accuracy order not lower than 4th order, the Taylor expansion analysis of (47) and (48) will give

$$\tilde{R}_{i+1/2} - \tilde{R}_{i-1/2} = R'(\xi_i) + O(\Delta\xi^4)$$

Where the 4th order accuracy is achieved.

In order to achieve the highest order accuracy of R_I $(I = i-3/2, i-1/2, i+1/2)$ in a least stencil not wider than the total width of the WENO stencils, for example, the stencil $S = (x_{i+r}, x_{i+r+1}, \cdots, x_{i+s})$ for all $\frac{\partial u}{\partial \eta}|_I$, $I = i-3/2, i-1/2, i+1/2$, we give the following formulas,

$$\mu_I = \sum_{l=m}^{n} C_l^I \mu_{i+l}, \ m = -2, n = 1, \tag{50}$$

$$\frac{\partial u}{\partial \xi}|_I = \frac{1}{\Delta\xi}\sum_{l=r}^{s} D_l^I u_{i+l}, \ r = -3, s = 2, \tag{51}$$

$$\frac{\partial u}{\partial \eta}|_I = \sum_{l=m}^{n} C_l^I \frac{\partial u}{\partial \eta}|_{i+l,j}, \ m = -2, n = 1, \tag{52}$$

where

$$\frac{\partial u}{\partial \eta}|_{i,j} = \frac{1}{\Delta\eta}\sum_{l=p}^{q} C_l^c u_{i,j+l}, \ p = -2, q = 2, \tag{53}$$

The other terms are determined similarly.

By choosing different ranges for $(m, n), (r, s), (p, q)$ and different coefficients C_l^I, D_l^I, C_l^c, one can obtain the different order accuracy of the viscous terms.

One principle of choosing $(m, n), (r, s), (p, q)$ is to ensure the approximation of $\frac{\partial R}{\partial \xi}|_i$ (Eq.(47))is a central differencing. $(m, n) = (-2, 1), (r, s) = (-3, 2), and\ (p, q) = (-2, 2)$, and the coefficients C_l^I, D_l^I, C_l^c are given in Tables 1-3.

Table 1: The coefficients of C_l^I

I	C_{-2}^I	C_{-1}^I	C_0^I	C_1^I
$i-3/2$	5/16	15/16	-5/16	1/16
$i-1/2$	-1/16	9/16	9/16	-1/16
$i+1/2$	1/16	-5/16	15/16	5/16

Table 2: The coefficients of D_l^I

I	D_{-3}^I	D_{-2}^I	D_{-1}^I	D_0^I	D_1^I	D_2^I
$i-3/2$	71/1920	-141/128	69/64	1/192	-3/128	3/640
$i-1/2$	-3/640	25/384	-75/64	75/64	-25/384	3/640
$i+1/2$	-3/640	3/128	-1/192	-69/64	141/128	-71/1920

5.3 Implicit Time Integration

The time dependent governing equations are solved using dual time stepping method suggested by Jameson[42]. To achieve high convergence rate, the implicit pseudo time marching scheme is used with the unfactored Gauss-Seidel line relaxation. The physical temporal term is discretized implicitly using a three point, backward differencing as the following (The prime is omitted hereafter for simplicity):

$$\frac{\partial \mathbf{Q}}{\partial t} = \frac{\mathbf{3Q^{n+1} - 4Q^{n} + Q^{n-1}}}{2\Delta t} \tag{54}$$

where $n-1$, n and $n+1$ are three sequential time levels, which have a time interval of Δt. The first-order Euler scheme is used to discretize the pseudo temporal term to enhance diagonal dominance. The semi-discretized equations of the governing equations are finally given as the following:

$$\left[\left(\frac{1}{\Delta\tau} + \frac{1.5}{\Delta t}\right) I - \left(\frac{\partial R}{\partial \mathbf{Q}}\right)^{n+1,m}\right] \delta\mathbf{Q^{n+1,m+1}} = \mathbf{R^{n+1,m}} - \frac{\mathbf{3Q^{n+1,m} - 4Q^{n} + Q^{n-1}}}{\mathbf{2\Delta t}} \tag{55}$$

where the $\Delta\tau$ is the pseudo time step, R is the net flux evaluated on a grid point using the fifth-order WENO scheme and the fourth-order central differencing scheme[30]. The implicit left hand side of Eq.(55) only affects the convergence behavior not the accuracy of the solution, which is determined by the right hand side of Eq.(55).

6 Results and Discussion

6.1 3D Subsonic Flat Plate Turbulent Boundary Layer Flow

The subsonic flat plate is used to validate the performance of the DDES scheme. The mesh size is $181 \times 81 \times 65$. The y^+ of the first cell center to the wall is kept less then 1.0. The mesh can be observed in Fig. 1. The Reynolds number is 4×10^6 based on the length of the plate. The inlet Mach

Table 3: The coefficients of C_l^c

C_{-2}^c	C_{-1}^c	C_0^c	C_1^c	C_2^c
1/12	-8/12	0	8/12	-1/12

number is 0.5.

As shown in Fig. 2, the computational results of the DDES scheme agree well with the law of the wall. They are slightly better than the results using S-A model alone in the transition region from the linear viscous sublayer to log layer.

6.2 3D Transonic Channel Flow

In this paper, the flow in a transonic channel is simulated, using both DES and DDES models, to study the shock wave/turbulent boundary layer interaction, which is analyzed experimentally in reference[43]. The channel is made of two straight side walls, a straight top wall, and a varying shape in span-wise direction for a bottom wall. The section tested on [44] has an entrance of 100mm in height by 120mm in width. Fig. 3 shows the topology of the duct's shape.

For the computation, the inlet the boundary conditions are set as fixed total pressure, total temperature and flow angles. At the outlet a fixed static pressure is specified. On the walls, the boundary conditions are set as no-slip adiabatic wall boundary condition. The flow for both DES and DDES models is calculated with a Reynolds number of 11.3×10^6 based on the throat's height and an inlet Mach number of 0.502.

Two mesh sizes are used for the DES calculation of $91 \times 61 \times 61$ and $136 \times 91 \times 91$, and three mesh sizes are used for the DDES calculation of $91 \times 61 \times 61$, $136 \times 91 \times 91$ and $211 \times 91 \times 91$. The meshes are mostly uniformly distributed in the horizontal direction except for the bump area, where the mesh is clustered to better resolve the shock wave. In the same way, the clustering also appears near the four walls of the duct to resolve the boundary layer. Fig. 3 shows the 3D mesh of the transonic channel.

A non-dimensional time step of 0.05 was used for the cases. The non-dimensional time is defined as $\bar{t} = \frac{t}{D/U_\infty}$, where D is the throat height. The computation begins with a uniform flow field. The convergence history within a typical physical time step is shown in Fig. 4, with the residual reduced typically by 2-3 orders of magnitude.

Fig. 5 and Fig. 6 show the computed instantaneous shock wave structure using the baseline mesh illustrated by Mach contours at 3 span-wise planes for the DES and DDES simulations respectively. Fig. 7 shows the result of the Mach number contours for the experiment [44] which are to be compared with those of Fig. 5 and Fig. 6. The location of the planes from the back side wall are $Z = 60mm$, $Z = 75mm$ and $Z = 90mm$, with the one located at $Z = 60mm$ being the central plane of the channel. In order to achieve the same location of the shock as in the experiment, the value of $\frac{p_{out}}{p_t} = 0.59$ is used for both DES and DDES. Using the baseline mesh, both the DES and DDES simulations have results in the shock wave structure very similar to that of the experiment, as shown in Fig. 7.

Compare the DES and DDES results at the plane $Z = 60mm$, the boundary layer of DDES is thinner than that of DES and agrees better with the experiment. The major difference between the results of DES and DDES simulations can be seen in plane $Z = 90mm$, where DES shows a thick layer with an area of separation significantly larger than the experiment. When looking at the DDES results, the separation is substantially reduced and agrees better with the experiment.

The surface shear stress flow are also plotted in this study and are found in Fig. 8 and Fig. 9. They show three faces of the channel, the top wall and both of the side walls. The results agree well with the experiment[44] observed in Fig. 10. On side A, both DES and DDES predict very well the top corner separation caused by the strong normal shock interaction with the corner boundary layer. On the lower part, the DDES predicts a little better the overall flow blockage due to the lower boundary layer separation and reattachment line. On the top wall, both DES and DDES capture the two side wall corner vortices well. On the side wall B, both the DES and DDES over predict the upper corner separation size, but the DDES gives better results in the rest of the area with no other separation lines as shown by the experiment. The DES has some separation/reattachment line near both the upper and lower walls outside the large upper wall corner separation zone.

The mesh refinement study with the mesh sizes mentioned above shows that DES is mesh dependent (grid density), given that the finner the mesh near the walls, the less agreement with the experimental results. This is expected to be resolved with the use of DDES as indicated by Sparlat[25].

Fig. 11 shows a plot of the computational isentropic Mach numbers on the top wall on plane $Z = 60mm$ of the transonic channel to study the convergence of the solution based on mesh refinement. Fig. 11 shows that the DDES solution is converged from the coarse mesh of $91 \times 61 \times 61$ to the finest mesh of $211 \times 91 \times 91$, whereas the DES solution is varied significantly from the coarse mesh of $91 \times 61 \times 61$ to the refined mesh of $136 \times 91 \times 91$. This results validate that the DDES is more mesh independent then the DES.

7 Conclusions

The shock/wave turbulent boundary layer interaction is studied by using a DDES simulation with low diffusion E-CUSP scheme [28] and fifth-order WENO scheme. A 4th order central differencing is used for the viscous terms.

The Delayed-Detached-Eddy Simulation (DDES) was suggested by Spalart in 2006 to fix a problem with the DES model. The transition from the RANS model to LES in DES is not grid spacing independent, therefore a blending function is introduced to the recently developed DDES model to overcome this shortcoming. The validation of the DDES method is performed by the simulation of the flow field of a 3D subsonic flat plate turbulent boundary layer. The computational results of the DDES scheme agree well with the law of the wall.

For a 3D transonic duct with a baseline grid of $91 \times 61 \times 61$, the computed shock/wave structure for three span wise planes agrees better with experiment using DDES compared to the results of DES near the walls of the channel. The computation of mesh refinement indicates that the grid density has significant effects on the results of DES, while being resolved by applying DDES simulation.

References

[1] J. Smagorinsky, "General Circulation Experiments with the Primitive Equations, I. The Basic Experiment," *Monthly Weather Review*, vol. 91, pp. 99–164, 1963.

[2] D. Lilly, "The Presentation of Small-Scale Turbulent in Numerical Simulation Experiments," *IBM Scientific Computing Symp. on Environmental Sciences*, p. 195, 1967.

[3] M. Germano, U. Piomeli, P. Moin, and W. Cabot, "A Dynamic Subgrid-scale Eddy Viscosity Model," *Physics of Fluids A*, vol. 3, pp. 1760–1765, July 1991.

[4] U. Piomeli, W. Cabot, P. Moin, and S. Lee, "Subgrid Scale Backscatter in Turbulent and Transitional Flows," *Physics of Fluids A*, vol. 3, pp. 1766–1771, July 1991.

[5] J. Deardorff, "A Numerical Study of Three Dimensional Turbulent Channel Flow at Large Reynolds Numbers," *Journal of Fluid Mechanics*, vol. 41, pp. 453–480, 1970.

[6] T. Kawamura and K. Kuwahara, "Computation of High Reynolds Number Flow Around a Circular Cylinder with Surface Roughness." AIAA Paper-84-0340, 1984.

[7] F. Grinstein, "Dynamics of Coherent Structures and Transition to Turbulence in Free Square Jet." AIAA Paper-96-0781, 1978.

[8] J. P. Boris, "On Large Eddy Simulation Using Subgrid Turbulence Models, in Whither Turbulence? ," *Turbulence at the Crossroads, edited by J.L. Lumley, New York: Springer-Verlag*, 1990.

[9] J. Boris, F. Grinstein, E. Oran, and R. Kolbe, "New Insights into Large Eddy Simulation," *Journal of Fluid Mechanics*, vol. 41, pp. 453–480, 1970.

[10] Boris, J., " More for LES: A Brief Historical Perspective of MILES," *Implicit Large Eddy Simulation, Editors: F. F. Grinstein, L. G. Margolin, and W. J. Rider*, vol. Cambridge University Press, pp. 9–38, 2007.

[11] Y.-Q. Shen and G.-C. Zha, "Comparison of High Order Schemes for Large Eddy Simulation of Circular Cylinder Flow." Submitted to 47th AIAA Aerospace Sciences Meeting and Exhibit, Jan., 2009.

[12] Y.-Q. Shen and G.-C. Zha, "Comparison of High Order Schemes for Large Eddy Simulation of Circular Cylinder Flow." AIAA-2009-0945, Submitted to Journal of Computational Physics, 2009.

[13] P. Spalart, W.-H. Jou, M. Strelets, and S. Allmaras, "Comments on the Feasibility of LES for Wings, and on a Hybrid RANS/LES Approach." Advances in DNS/LES, 1st AFOSR Int. Conf. on DNS/LES, Greyden Press, Columbus, H., Aug. 4-8, 1997.

[14] P. R. Spalart, "Young-Person's Guide to Detached-Eddy Simulation Grids." NASA/CR-2001-211032, 2001.

[15] P. R. Spalart, "Topics in Detached-Eddy Simulation."

[16] B.-Y. Wang and G.-C. Zha, "Dettached Eddy Simulation of Transonic Airfoil Limited Cycle Oscillation with High Order WENO Scheme." AIAA Paper 2009-1507, the 47th AIAA Aerospace Sciences Meeting and Exhibit, Orlando, Florida, 5 - 8 Jan 2009.

[17] B.-Y. Wang and G.-C. Zha, "Detached-Eddy Simulation of a Co-Flow Jet Airfoil at High Angle of Attack." AIAA Paper 2009-4015, 2009.

[18] A. Tarvin, M. Shur, M. Strelets, and P. Spalart, "Detached-Eddy Simulations Past a Circular Cylinder," *Flow Turbulence and Combustion*, vol. 63, 1999.

[19] J. R. Forsythe, K. A. Hoffmann, and K. D. Cummings, R. M. Squires, "Detached-Eddy Simulations with Compressibility Corrections Applied to Supersonic Axisymmetric Base Flow," *Journal of Fluids Engineering*, vol. 124, 2002.

[20] A. Viswanathan, K. Klismith, J. Forsythe, and K. D. Squires, "Detached-Eddy Simulation around a Forebody at High Angle of Attack." AIAA-2003-0263, 2003.

[21] K. D. Squires, "Detached-Eddy Simulation: Current Status and Perspectives."

[22] K. D. Squires, J. R. Forsythe, and P. R. Spalart, "Detached-Eddy Simulation of the Seperated Flow Around a Forebody Cross-Section."

[23] R. P. Hansen and J. R. Forsythe, "Large and Detached Eddy Simulation of a Circular Cylinder Using Unstructured Grids." AIAA Paper 2003-0775, Jan. 2003.

[24] P. Subbareddy and G. V. Candler, "Numerical Investigations of Supersonic Base Flows Using DES." AIAA Paper 2005-0886, Jan. 2005.

[25] P. Spalart, S. Deck, M. Shur, and K. Squires, "A New Version of Detached-Eddy Simulation, Resistant to Ambiguous Grid Densities," *Theoritical and Computational Fluid Dynamics*, vol. 20, pp. 181–195, 2006.

[26] C. Rumsey, "Successes and Challenges for Flow Control Simulations." AIAA Paper 2008-4311,AIAA 4th Flow COntrol Conference, Seattle, Washington, 23-26 June 2008.

[27] F. Menter and M. Kuntz, "Adaptation of Eddy-Viscosity Turbulence Models to Unsteady Separated Flow Behind Vehilces, *The Aerodynamics of Heavy Vehicles: Trucks, Buses and Trains, Edited by McCallen, R. Browand, F. and Ross, J. ," Springer, Berlin Heidelberg New York, 2004*, 2-6 Dec. 2002.

[28] G.-C. Zha, Y. Shen, and B. Wang, "Calculation of Transonic Flows Using WENO Method with a Low Diffusion E-CUSP Upwind Scheme." AIAA Paper 2008-0745, 46th AIAA Aerospace Sciences Meeting, Reno, NV, Jan. 2008.

[29] C.-W. Shu, "Essentially Non-Oscillatory and Weighted Essentially Schemesfor Hyperbolic Conservation Laws." NASA/CR-97-206253, 1997.

[30] Y.-Q. Shen, B.-Y. Wang, and G.-C. Zha, "Implicit WENO Scheme and High Order Viscous Formulas for Compressible Flows ." AIAA Paper 2007-4431, 2007.

[31] Y.-Q. Shen, G.-C. Zha, and X. Chen, "High Order Conservative Differencing for Viscous Terms and the Application to Vortex-Induced Vibration Flows." AIAA Paper 2008-4059, 38th AIAA Fluid Dynamics Conference and Exhibit, Seattle, Washington, 23 - 26 June, 2008.

[32] Y.-Q. Shen, G.-C. Zha, and B.-Y. Wang, "Improvement of Stability and Accuracy for Weighted Essentially Nonoscillatory Scheme," *AIAA Journal*, vol. 47, pp. 331–344, No.2, 2009.

[33] Y.-Q. Shen and G.-C. Zha, "Improvement of the WENO Scheme Smoothness Estimators." AIAA Paper 2008-3993, 38th AIAA Fluid Dynamics Conference and Exhibit, Seattle, Washington, 23 - 26 June, 2008.

[34] P. Spalart and S. Allmaras, "A One-equation Turbulence Model for Aerodynamic Flows." AIAA-92-0439, 1992.

[35] R. P. Hansen and J. Forsythe, "Large and Detached Eddy Simulation of a Circular Cylinder Using Unstructured Grids." AIAA-2003-0775, 2003.

[36] M. Shur, P. Spalart, M. Strelets, and A. Travin, "Detached-Eddy Simulation of an Airfoil at High Angle of Attack", 4th Int. Symp. Eng. Turb. Modelling and Measurements, Corsica." May 24-26, 1999.

[37] B. Wang, "Detached-eddy Simulation of Flow Non-linearity of Fluid-Structural Interactions Using High Order Schemes and Parallel Computation." Ph.D. Thesis, University of Miami, November 2008.

[38] P. Roe, "Approximate Riemann Solvers, Parameter Vectors, and Difference Schemes," *Journal of Computational Physics*, vol. 43, pp. 357–372, 1981.

[39] B.-Y. Wang and G.-C. Zha, "Comparison of a Low Diffusion E-CUSP and the Roe Scheme for RANS Calculation." AIAA Paper 2008-0596, 46th AIAA Aerospace Sciences Meeting and Exhibit, Jan. 7-10, 2008.

[40] J. R. Edwards, "A Low-Diffusion Flux-Splitting Scheme for Navier-Stokes Calculations." AIAA Paper 95-1703-CP, June, 1995.

[41] J. R. Edwards, "A Low-Diffusion Flux-Splitting Scheme for Navier-Stokes Calculations," *Computer & Fluids*, vol. 6, pp. 635–659, 1997.

[42] A. Jameson, "Time Dependent Calculations Using Multigrid with Applications to Unsteady Flows Past Airfoils and Wings." AIAA Paper 91-1596, 1991.

[43] J. M. Délery, "Experimental investigation of turbulence properties in transonic shock/boundary-layer interaction," *AIAA Journal*, vol. 21, 1983.

[44] R. Benay, J. M. Délery, and T. Pot, "Etude expérimentale d'une interaction onde de choc-couche limite en canal tridemensionnel. propriété du champ moyen," Tech. Rep. Rapport Technique no 70/7078 AN, ONERA, 1986.

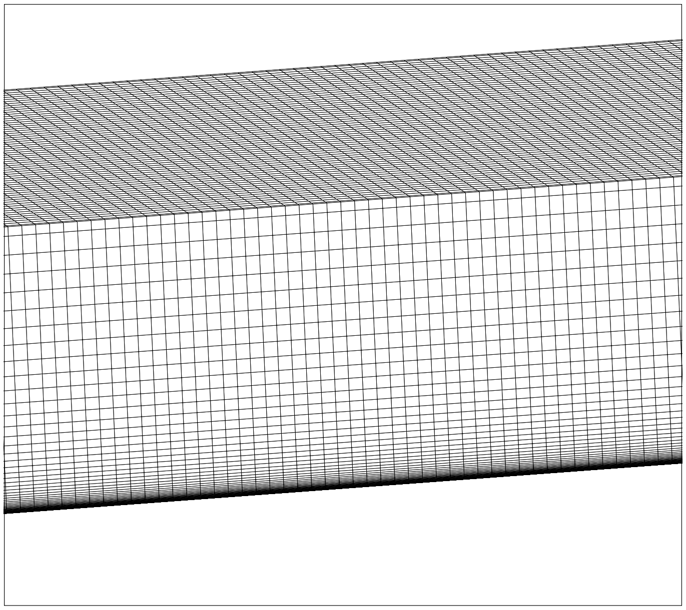

Figure 1: 3D view of the mesh for the subsonic flat plate

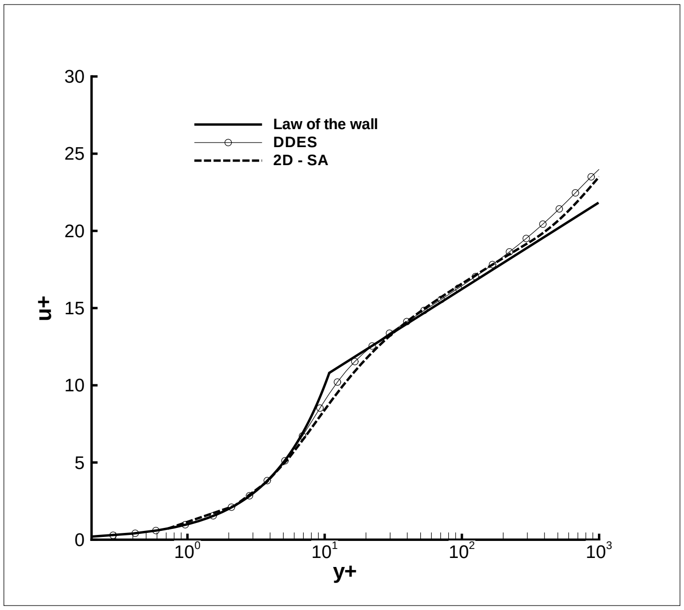

Figure 2: Law of the wall of a subsonic flat plate

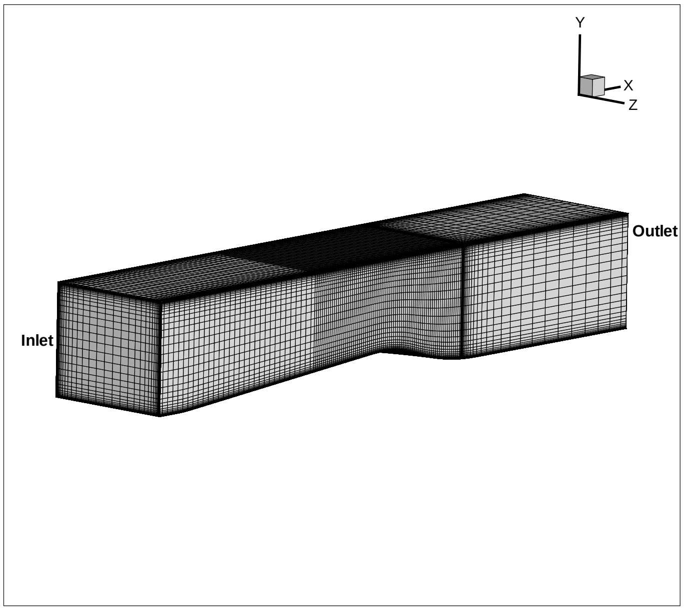

Figure 3: The computational grid of the transonic channel

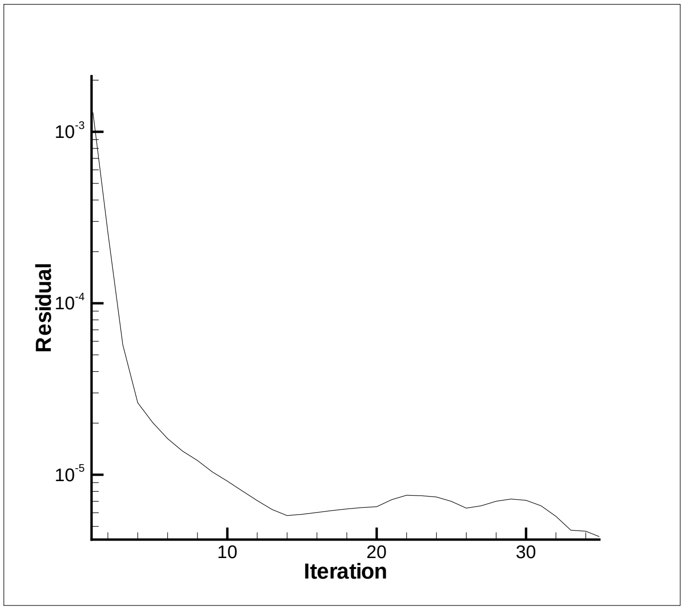

Figure 4: Convergence history within a typical time step for transonic duct

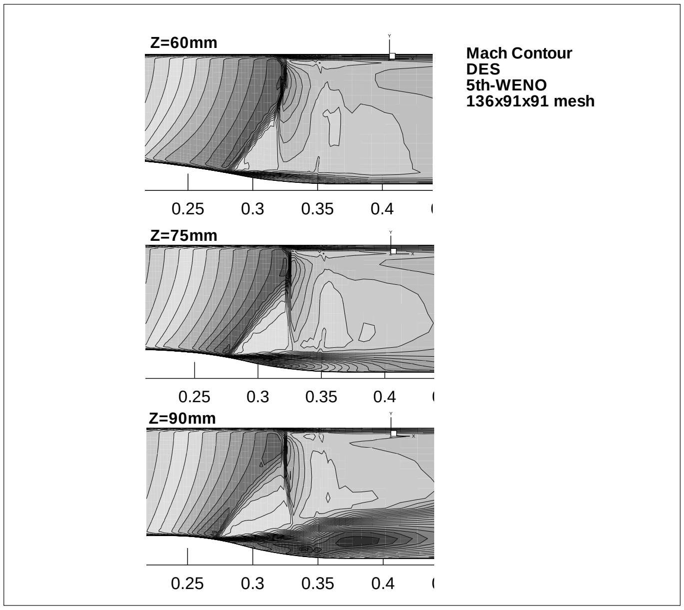

Figure 5: Transonic duct Mach number contours for DES

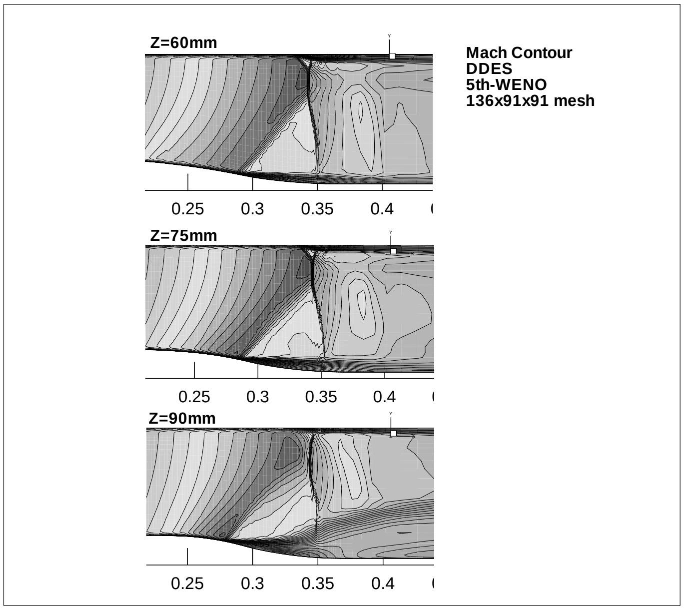

Figure 6: Transonic duct Mach number contours for DDES

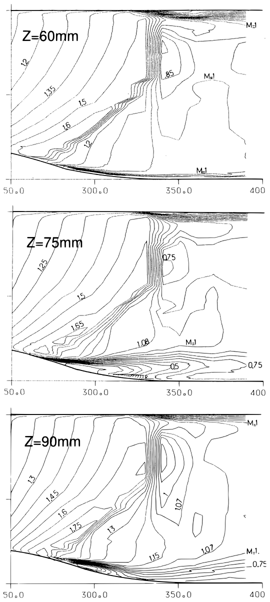

Figure 7: Transonic duct Mach number contours from experiment

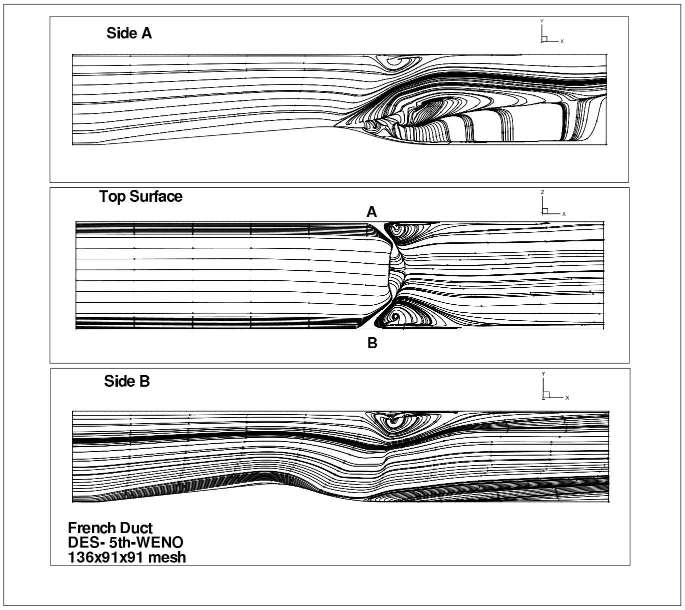

Figure 8: Transonic duct surface shear stress lines on walls for DES

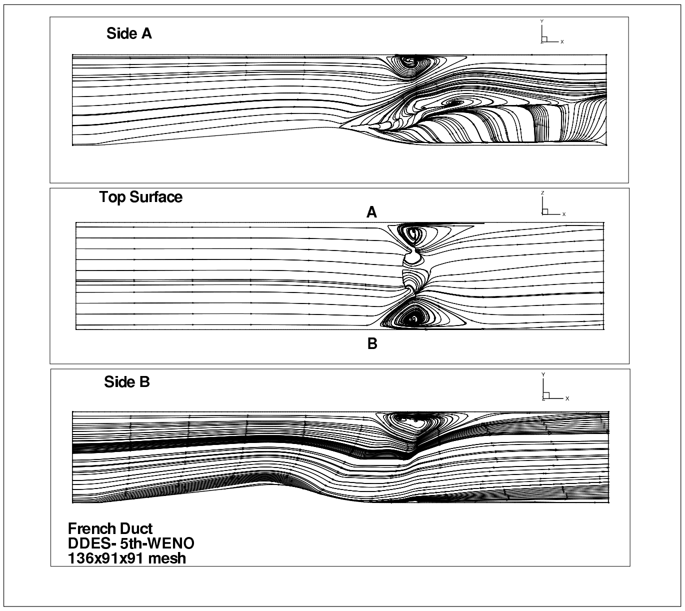

Figure 9: Transonic duct surface shear stress lines on walls for DDES

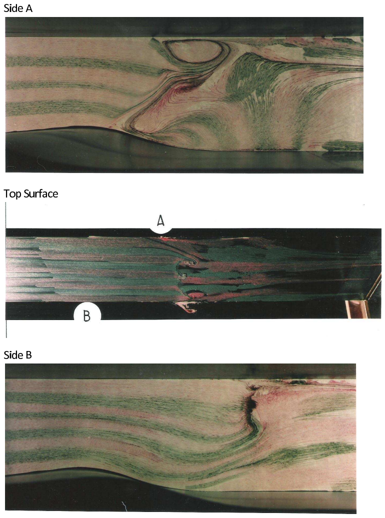

Figure 10: Transonic duct surface experimental shear stress for top, side A and side B walls[44]

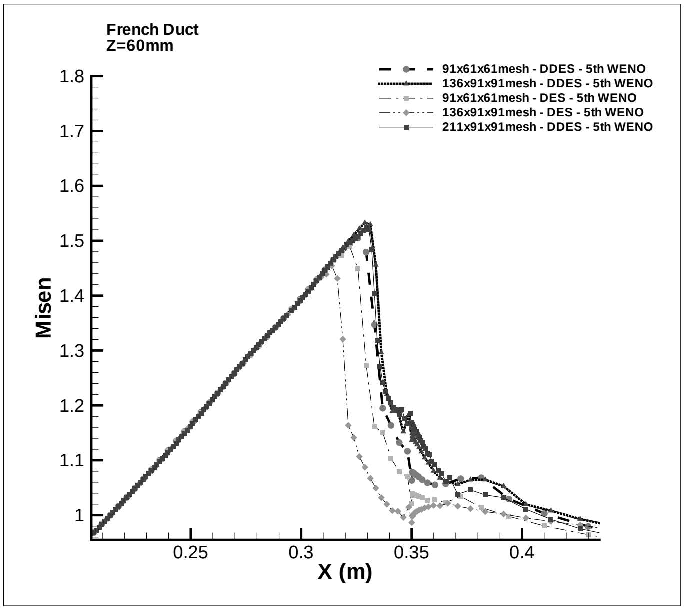

Figure 11: Isentropic Mach number on top wall of transonic duct at plane Z=60mm, experiment data[44]